A COMPUTATIONAL STUDY ON BLADE-VORTEX INTERACTION FOR COAXIAL ROTORS IN HOVER USING A NOVEL HIGH-ORDER SCHEME

HAN Shaoqiang[1,*], SONG Wenping[2], HAN Zhonghua[2]

[1]Tianfu Engineering-oriented Numerical & Software Innovation Center, College of Computer Science, Sichuan University, Chengdu 710071, P. R. China.
[2]Northwestern Polytechnical University, Xi'an 710071, P. R. China

Abstract

Accurate prediction of tip vortices is crucial for mechanism study on the blade-vortex interaction(BVI) for coaxial rotors. A new high-order scheme (WENO-K) proposed by our research group is employed to minimize numerical dissipation and extended to numerical simulation of unsteady flows dominated by tip vortices around hovering coaxial rotors. WENO-K is referred to as an adaptively optimized WENO scheme with Gauss-Kriging reconstruction, and its advantage is to reduce dissipation in smooth regions of flow while preserving high-resolution around discontinuities. Here WENO-K scheme is adopted to reconstruct left and right state values within the Roe Riemann solver updating the inviscid fluxes on a structured dynamic overset grid. To minimize the accuracy loss for high-order reconstruction on artificial boundaries of overset grid, a method of multilayer fringes is proposed to carry out interpolation between background grid and blade grid. A conservative method is developed for the flow variable interpolation in the overset grid interface. High-accurate numerical simulation of vortex wake structure over a coaxial rotor was carried out. The results indicates that the tip vortex structure and its unsteady generation, development and evolution process can be completely simulated and preserved by WENO-K scheme, and the pressure impulses on the blade caused by BVI can also be well captured.

Keywords: Coaxial rotor; blade-tip vortex; high-order scheme; blade-vortex interaction; unsteady flow

1. Introduction

Featured by outstanding performances such as high maneuverability, high speed, high efficiency and compactness, coaxial helicopter has grown as an important branch for advanced high-speed helicopters in the future [1]. As the key component of coaxial helicopter to generate lift and control forces, coaxial rotor stirs more complicated unsteady vortical interaction flowfields than conventional single rotor. The development of tip vortex is highly unsteady, and continues to evolve into a very complex vortical structure, along with some complex flow such as blade-vortex interaction (BVI), vortex-vortex interaction and vortex-fuselage interaction, which greatly affects flying qualities, noise radiation and vibrations of coaxial helicopters [2]. Therefore, it is very important to study the numerical simulation method and mechanism of vortex flow over coaxial rotors. Blade-tip vortex structures are very sensitive to numerical dissipation, and thus high-accurate capture of tip vortex structures have always been an academic puzzle [3]. Therefore, we propose to develop a numerical method for blade-tip vortices of coaxial rotor based on a novel high-order and low-dissipation scheme on structured overset grids, and conduct a computational study of BVIs.

1.1 Complex flow around coaxial rotors

Flowfield around a conventional single rotor generally contains the following complex flow characteristics [1]-[5]:

- The local inflow velocity of rotor blade varies linearly along the spanwise, so there exists both incompressible flow area near rotor hub and transonic flow area near blade tip. At high-speed forward flight, three-dimensional unsteady transonic flow will appear on advancing blade, while

flow separation and dynamic stall easily occur on the retreating blade.

- The tip vortex generated during the rotation of blades will roll up in the flowfield and form a spiral vortex structure. BVI will occur when tip vortex collides with the blade, which seriously affects the aerodynamic performance and aeroacoustic characteristics of rotors.

There exists unique and stronger interference flow phenomena between the upper and lower rotors of coaxial rotors [6] except for the above flow characteristics:

- When the blades of the upper and lower rotors get close to each other, the air flow pipe around the blades narrows, resulting in an increase in the local velocity, which leads to a decrease in the pressure on the lower surface of the upper blade and the upper surface of the lower blade. Then instantaneous impulse interference will appear periodically, which is called "thickness effect".

- When the upper and lower rotor blades are close to / away from each other, the attached vortex circulation caused by blade load will produce up wash flow / down wash flow to the other blade, and gradually increase with the approach of the two blades. The above induced speed and direction changes make the aerodynamic forces of the blade change synchronously, and form a continuous aerodynamic interference. This interference phenomenon is related to the aerodynamic load of the blade, which is called "load effect".

- The tip vortex generated by the upper rotor moves downward in a spiral shape. Firstly, it collides with the lower rotor blade, resulting in the phenomenon of "upper / lower rotor BVI". The above aerodynamic interference is intensive due to the small distance between the upper and lower rotors for rigid coaxial rotor.

- After the tip vortex generated by the upper rotor moves downward for a certain distance, it will collide, wind, fuse and break with the tip vortex of the lower rotor, forming a "vortex / vortex interference". This interference is strongly unsteady.

Obviously, the wake vortex structure of coaxial rotor is the key factor to produce complex interference flow field. The vortex structure are relatively compact, and the transport process is accompanied by viscous diffusion and BVIs that is extremely easy to be dissipated numerically [7]-[8], so accurate and high-resolution simulation of vortex structure for coaxial rotor is challenging.

1.2 Research status of numerical methods for flow simulation of coaxial rotors

As for the numerical simulation method of flow around coaxial rotors, a lot of meaningful research work has been carried out at home and abroad. Leishman et al. first developed the momentum-blade element theory to predict the aerodynamic characteristics of coaxial rotors [9]-[11]. Andrew [12] and bagai [13] used the wake model to study the aerodynamic characteristics of coaxial rotors. Kim and brown [14][15] developed a vortex transport model for coaxial rotors. These methods have the advantage of high efficiency, but they can not accurately simulate details of flow field interference. Barbely [16] used the unstructured solver RotUns to capture more than three cycles of vortical wake for HC1 coaxial rotor at forward flight, however, no BVIs is captured. Xu Heyong and Ye Zhengyin [17]-[18] studied the hovering flowfield and aerodynamic interference of coaxial rotor helicopter by solving Euler equation and NS equations, and spatial discretization is conducted by using second-order central finite volume method. Ye Liang and xu Guohua [19] numerically simulated the flow field and aerodynamic characteristics of coaxial rotors by using third-order upwind scheme and introducing adaptive mesh technique on unstructured grid. Zhu Zheng and Zhao Qijun [20] studied the unsteady flow interference mechanism of rigid coaxial rotor in hover on structured overset grid, and obtained unsteady aerodynamic forces of hovering coaxial rotor caused by blade-tip vortex interference.

At present, the main difficulty in the numerical simulation of coaxial rotor flow is the exccessive dissipation of numerical method. Thus wake vortex structure captured is relatively rough, and the variation laws of unsteady aerodynamic forces and mechanism of vortical flow interference of coaxial rotor is not clear. The detailed dynamic evolution of tip vortex and other complex interference can not be accurately simulated by only adopting low-order numerical method or wake model. Therefore, developing high-accuracy and low-dissipation CFD methods is the key point to simulate the generation, development, evolution and interference of wake vortices for coaxial rotor.

2. Computational grid and numerical method
2.1 Structured overset grid system

High-quality grid and appropriate treatment for overset boundaries contribute to preserve the accuracy of flow simulation by using high-order schemes for helicopter rotors.

Take a four-blade coaxial rotor for example, the dynamic overset grid system used for discretization of computational domain are composed of a static Cartesian background grid and four blade grids with rotational motion as shown in Figure 1(a) and (b). Figure 1(c) shows the structured C-H body-fitted grid generated by using transfinite interpolation. Figure 2 gives cut away views of refined region on background grid for wake capture, where the grid keep approximately uniform and strictly orthogonal to guarantee good performance of spatial schemes. According to the widely accepted practice [4] of grid generation for numerical simulation of rotor flows, we take strict control of the cell height in the first layer (y+<1), the distribution of grid on blade tip (Δ<0.2%c), and the cell size in the wake region of interest (Δ<5%c).

The grid system of "background grid + blade grid" has following advantages:

*   Generate grids separately in different sub regions, which ensures the quality of grids;

*   When the blade is in motion of translation and rotation, the whole blade grid moves with the blade, and there is no need to conduct grid regeneration;

*   All blade grids are only overlapping with background mesh, which greatly simplifies the overset relationship and improves the efficiency of grid assembly process.

| (a) Global view of background grid and blade grids | (b) Local view of background grid and blade grids | (c) Cut away view of C-H grid for rotor blade |

Figure 1 Structured overset grid system for a coaxial rotor.
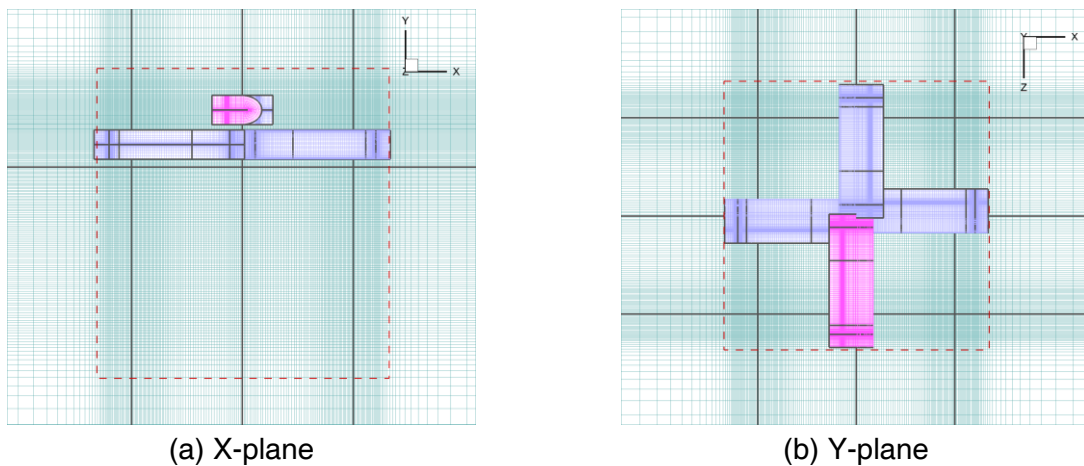
| (a) X-plane | (b) Y-plane |

Figure 2 Cut away view of refined region on background grid for wake capture.

The overset relationship between blade grid and background grid needs to be identified after grid generation. The hole boundary cells need to be redetermined at every physical time step by using the Hole Map method [21]. First, a virtual Cartesian grid called Hole Map is generated to cover the blade. Second, those background grid cells within the Hole Map are defined as hole cells. Finally, the outer boundary of hole is the new approximate hole boundary. For the sake of simplicity, Figure 3 gives a two-dimensional section view of hole and its boundary. Considering the WENO scheme requiring a big stencil to build the high-order spatial flux, multilayer artificial boundaries are proposed as shown

in Figure 3 to ensure no accuracy reduction for fifth-order reconstruction in the hole boundaries and the artificial external boundaries.

| (a) Hole boundaries | (b) Artificial outer boundaries |
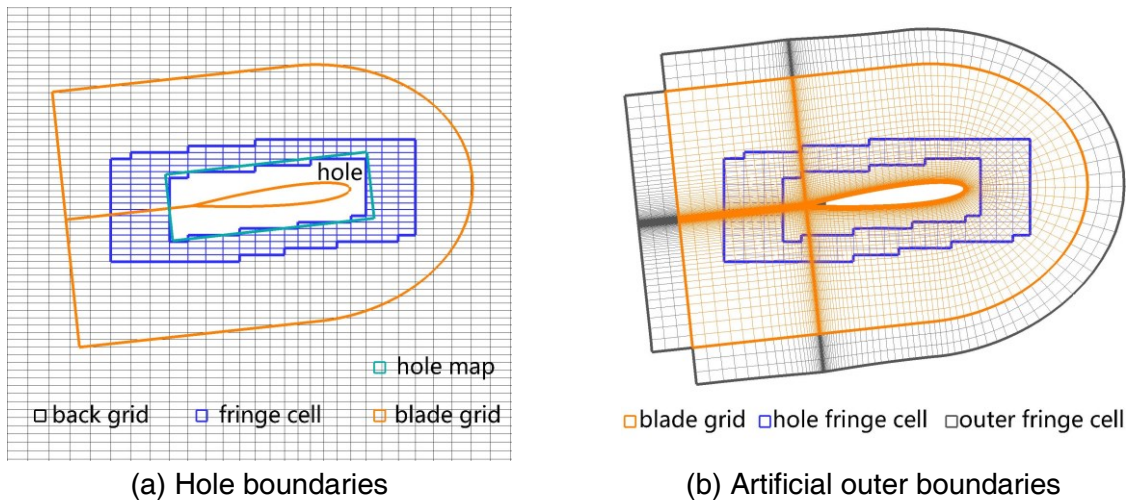
Figure 3 Schematic sketch of three-layer artificial boundaries on background grid and blade grid.

The flow variables on the artificial outer boundary cells in blade grid are interpolated from donor cells in background grid. Similarly, the flow variables on the hole boundary in background grid are provided by donor cells in blade grid. Here we proposed a multi-start distance decreasing method algorithm [22] to optimize the efficiency and avoid search failure. The multi-start distance decreasing method for identification of artificial boundaries and search of donor cells perform suitably and very efficiently on the background grid and blade grid with single block.

An conservative interpolation algorithm based on cell intersection is developed. This method firstly establishes the matching relationship between receiver cells and donor cells according to the spatial relationship between the overset grids, and then constructs intersections between matched grid cells through cell cutting. Then mass, energy, and momentum could be interpolated conservatively from donor cells to receiver cells.

2.2 Arbitrary partition of grid system for parallel computation

Here we introduce the process of arbitrary partition for grid system and parallel computation step by step in detail.

Step 1: Single-block grid generation. The initial grid system for a four-bladed rotor show in Figure 1 consists of a background grid and four blade grids, and the cell number of background grid is much larger than that of the blade grids. This kind of grid system limits the number of processors used for parallel calculation depending on blocks of grid to no more than 5 without considering load balancing.

Step 2: Arbitrary partition of grid system. In order to achieve efficient parallel numerical simulation considering automatic load balance, the blocks of grid system show in Figure 1 is averagely divided as shown in Figure 2 according to the number of processors available.

Step 3: Identification of cell-types and search of donor cells. Conduct the overset technique introduced in Section 2.1 on the initial grid system and save cell-types and interpolation relation for overset grid. This step goes fast enough by using the multi-start distance decreasing method.

Step 4: Allocate the overset information generated in Step 3 to the partitioned grid system according to the correspondence between single-block grid and multi-block grid.

Step 5: N sub-processors equally share the grid blocks and perform sub-iterations in parallel, and one main processor is responsible for data interaction between the sub-processors.

2.3 High-order and low-dissipation numerical method

There exists strong unsteady interferences between the upper and lower rotors even for hovering coaxial rotor. This paper solves the unsteady RANS equations. Under the framework of finite volume method, dual time-stepping, higher-order upwind scheme, SA turbulence model, multigrid technique,

unsteady preprocessing technique and efficient parallel computing based on MPI are adopted.

In order to improve the reconstruction accuracy of the inviscid flux on the interface, it is generally necessary to expand the template. For three-dimensional cases, the size of templates used for reconstruction increase sharply with the improvement of order of accuracy, which makes it difficult to guarantee the stability of reconstruction, especially for flows that contain discontinuities. When discretizing the inviscid flux, the variable reconstruction on the cell interface adopts the fifth-order WENO-K scheme [23]. On structured grids, it is easy to achieve a certain degree of decoupling in three dimensions, then three one-dimensional high-order reconstructions can be conducted to achieve high-order discretization of three-dimensional complex flow. The template contains the least number of grid elements, and the stability of the reconstruction will be significantly improved. This method is called the approximate higher-order finite volume method [24]-[25]. The approximate higher-order finite volume method ignores the transformation of the volume-averaged variables and surface-averaged variables, which allows the reconstruction process to be approximately decoupled in each direction of the structural grid. Strictly speaking, it can only reach a theoretical accuracy of the second-order, however, it performs good robustness and is widely used in applications. This method is simple to implement and spends low computational cost, and is very suitable for three-dimensional complex flow problems. In the case of poor mesh quality, it can avoid the occurrence of high-order negative volumes.

Unsteady RANS equations without any wake model are adopted to solve tip vortex. The viscous fluxes of URANS equations are discretized by the second-order central finite volume method, and the inviscid fluxes are approximated by the Roe flux difference splitting scheme [26] that features good robustness and high resolution. The reconstruction of the interface variables $W_{L,i+1/2}$ and $W_{R,i+1/2}$ from cell averages is the key for a finite volume method to obtain approximately high-order accuracy. Here reconstructions of primitive variables $Q = [\rho, u, v, w, p]^T$ are conducted by using third-order MUSCL scheme, fifth-order WENO-JS scheme and WENO-K scheme respectively.

We proposed the WENO-K scheme [23] with Gauss-Kriging reconstruction and an adaptively optimized hyper-parameter. WENO-K is easily to be implemented under the framework of WENO-JS, and it features lower dissipation for reconstruction on the same stencils as WENO-JS with only a small amount of additional computational cost.

Assume $q_{L,i+1/2}$ is a scalar component of $Q_{L,i+1/2}$, the fifth-order WENO-K interpolation is given by

$$q_{L,i+1/2} = \omega_0 q_{i+1/2}^{(0)} + \omega_1 q_{i+1/2}^{(1)} + \omega_2 q_{i+1/2}^{(2)} \tag{1}$$

where $q_{i+1/2}^{(k)}$ for k=0,1,2 are the extrapolated values obtained from cell averages $\bar{q}$ in the kth forth-order (only third-order for WENO-JS) sub stencil $S_k = (i-k, i-k+1, i-k+2)$ and are given by

$$\begin{cases} q_{i+1/2}^{(0)} = \left(\frac{1}{3} - \frac{1}{4}\theta\right)\bar{q}_{i-2} + \left(-\frac{7}{6} + 3\theta\right)\bar{q}_{i-1} + \left(\frac{11}{6} - \frac{11}{4}\theta\right)\bar{q}_i \\ q_{i+1/2}^{(1)} = \left(-\frac{1}{6} - \frac{1}{4}\theta\right)\bar{q}_{i-1} + \left(\frac{5}{6} - \frac{1}{3}\theta\right)\bar{q}_i + \left(\frac{1}{3} + \frac{7}{12}\theta\right)\bar{q}_{i+1} \\ q_{i+1/2}^{(2)} = \left(\frac{1}{3} + \frac{7}{12}\theta\right)\bar{q}_i + \left(\frac{5}{6} - \frac{1}{3}\theta\right)\bar{q}_{i+1} + \left(-\frac{1}{6} - \frac{1}{4}\theta\right)\bar{q}_{i+2} \end{cases} \tag{2}$$

where the interpolation coefficients containing θ is a simplification for results of Gauss-Kriging interpolation. After a series of complex error analysis, optimized hyper-parameter θ can be expressed as

$$\theta = \frac{6}{5} \frac{\bar{q}_{i-1} - 3\bar{q}_i + 3\bar{q}_{i+1} - \bar{q}_{i+2}}{\bar{q}_{i-1} - 15\bar{q}_i + 15\bar{q}_{i+1} - \bar{q}_{i+2}} \tag{3}$$

Table 1 gives the pseudo codes for formulas of optimized hyper-parameter θ, by which one can calculate the optimized hyper-parameter efficiently with troubled cells eliminated automatically. The

range of indicator a is determined by a large number of numerical tests and works well for most cases. It is obviously that the WENO-K scheme degenerates to WENO-JS when $\theta=0$ or in cells containing discontinuities.

Table 1 Pseudo codes for the new formulas of optimized hyper-parameters [23]

Cells for reconstruction	Pseudo codes for the optimized hyper-parameters
Three cells	$\theta = 0, \forall i = 1,\dots$ (indicating I_i is a troubled cell) For $i = 1,\dots,N$ Given I_i $a = \dfrac{\bar{q}_{i-1} - \bar{q}_{i+2}}{\bar{q}_{i+1} - \bar{q}_i}$ (indicator of troubled cells) If -6.5< a <5 (comfort zone) $\theta = \dfrac{6}{5}\left(1 - \dfrac{12}{15+a}\right)$ (calculation of hyper-parameters)

The expressions of nonlinear weights ω_k are the same as the WENO-JS method developed by Jiang and Shu (WENO-JS) [27].

The right value $q_{R,i+1/2}$ can be obtained by symmetry of the left and right states. It should be emphasized that FVM can only reach second-order accuracy especially for three-dimensional flow around complex boundaries. However, if the refined grid in wake region keeps nearly uniform and strictly orthogonal, an approximate high-order FVM can be obtained by performing high-order WENO reconstructions. The approximate high-order FVM features low dissipation, high resolution and high efficiency, which performs obviously better than MUSCL scheme for the capture of smooth flow structures and prediction of aerodynamic forces [28]-[32].

A full implicit dual-time stepping method with LU-SGS sub-iteration is adopted to advance the unsteady solution of the rotor flow in hover in time. Local time-stepping, implicit residual smoothing and multigrid method are applied to accelerate the convergence of sub-iterations.

3. Results and discussion

All simulations are carried out in parallel on TianHe-1(A) system of National Supercomputer Center in Tianjin. Each computing node is configured by 2 Intel Xeon CPUs (e5-2690 V4 @ 2.60GHz) with 14cores, namely, 28 processors per node.

The coaxial rotor model with a relatively simple blade shape is selected [33], and Table 2 gives the geometry parameters of the coaxial rotor model. The hovering coaxial rotor operates at the following condition: Mach number of blade tip is 0.363, Reynolds number based on the blade-tip chord length is 0.5×10^6, and three pitch angles(6°, 9°, 12°) of blade are studied. Wake prediction is the key point of numerical simulation under this flow condition. A comparative study was carried out by adopting third-order MUSCL scheme, fifth-order WENO-JS scheme and WENO-K scheme respectively.

The structured moving overset grid used for the test coaxial rotor model is shown in Figure 4. Size of background grid cell is 0.05c near blade tip and 0.1c between the upper / lower rotors. Distance from center point of the rotor disc to farfield is 25 times of the rotor diameter. The blade grid consists of $176 \times 60 \times 200$ grid cells and the background grid consists of $240 \times 240 \times 240$ grid cells. The total grid volume is about 22.3 million. The whole computing domain is divided into 112 grid blocks with nearly equal cell number of about 200000, and 112 processors are used for parallel simulation. 10 revolutions of unsteady simulation are conducted and each revolution of rotation is divided into 720 physical time steps with 20 sub-iterations for each time step, which gives at least a third-order sub-iteration drop between time steps.

6

Table 2 Parameters of the coaxial rotor.

Geometric parameters	Value
Number of blades N	2+2
Plane shape of blade	Rectangle
Profile airfoil of blade	NACA0012
Coaxial rotor solidity σ	0.2
Coaxial rotor radius R	0.38m
Rotor separation	0.26R
Chord of blade c	0.06m
Root cut of blade	0.21R
Twist of blade	None
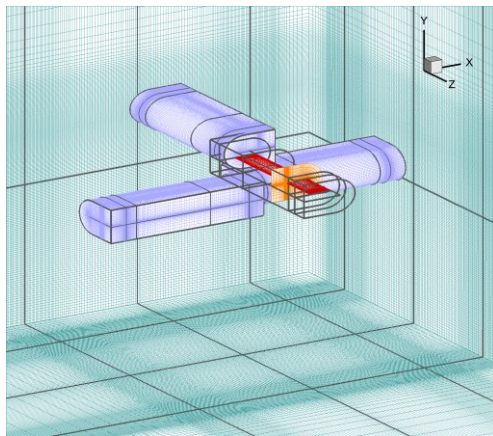
(a) Local view of grid system   (b) Cut away view of C-H grid for rotor blade
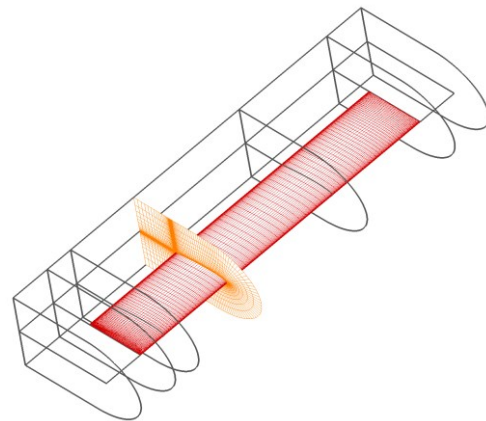
Figure 4 Computational grid system of the coaxial rotor model.

3.1 Validation of numerical methods and codes

Figure 5 shows the comparison between the calculated and experimental values of the thrust/torque coefficients in hover at three different pitch angles. The calculations are in good agreement with the experiment, and the fifth-order WENO-K scheme gives the most accurate results. The maximum error of the thrust coefficient is 6.8%, which verifies the applicability and correctness of developed methods and programs for numerical simulation of flow around coaxial rotor in hover.
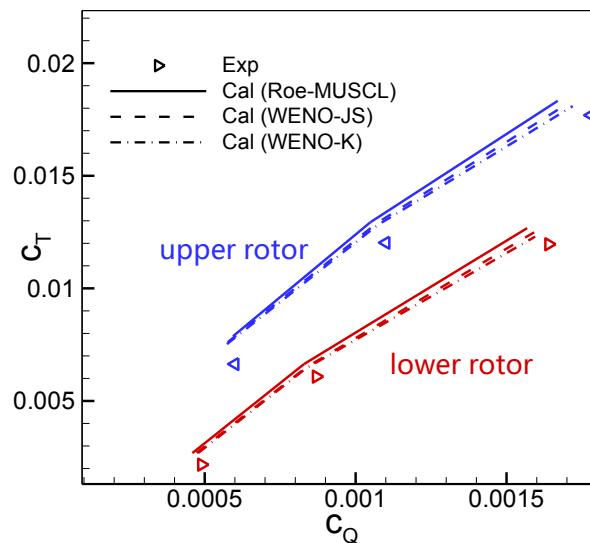
Figure 5 Comparison of calculation and experiment for thrust/torque coefficients of coaxial rotors in hover.

3.2 Visualization of blade-tip vortices

Figure 6 shows the comparison of tip vortices visualized by iso-surface of q-criterion (q=0.01) and contours of vorticity magnitude at pitch angle of 6°. Because the lower rotor is in the downwash of the upper rotor, the lift of lower rotor is smaller with weaker tip vortices that dissipate out faster. Due to the excessive dissipation, Roe-MUSCL scheme totally can't capture the interference of the tip vortex between the lower/upper rotor, and the max wake age of visible tip vertices are less than 180°. WENO-JS scheme can hardly capture the vortex-vortex interference, and the max wake age of visible tip vertices are about 360°. WENO-K scheme preserve tip vortices to about 540° of wake age, and there are obvious winding and breaking phenomena between the tip vortices of the upper and lower rotors.

(a) 3rd-order MUSCL	(b) 5th–order WENO-JS	(c) 5th–order WENO-K
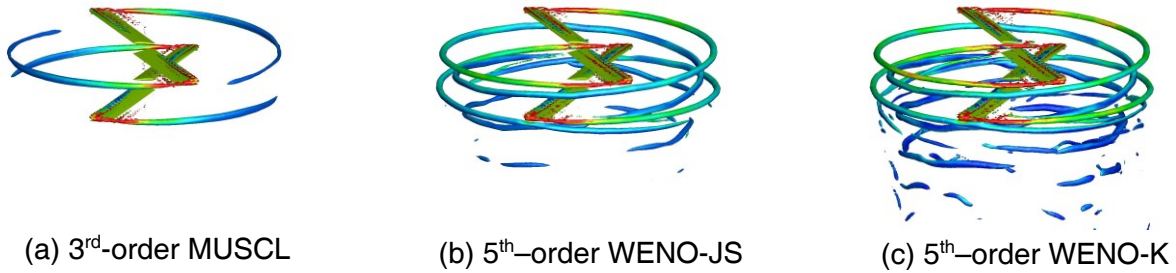
Figure 6 Comparison of tip vortex for coaxial rotor in hover (θ=6°). Vortices rendered with the iso-surface of q-criterion and contours of vorticity magnitude.

Figure 7 shows the instantaneous vorticity contours on cutting plane. Near to the rotors, the images show the orderly downstream procession of the tip vortices and their associated inner wake sheets, in which tip vortex dominates the intensity of the whole vortex structure. A double-tube structure formed by the tip vortices of the coaxial rotor develops spirally downward and show a trend of contraction, and the vortex wake of the upper rotor contracts faster on the inner side of the vortex trajectory of lower rotor. The vorticity captured by the WENO-K scheme is more intensive than that of the other schemes at the same wake age, and the whole wake structure is also clearer. In addition, it should be noted that the inward contraction of lower rotor wake is weaker due to squeeze of the upper rotor wake.

(a) 3rd-order MUSCL	(b) 5th–order WENO-JS	(c) 5th–order WENO-K
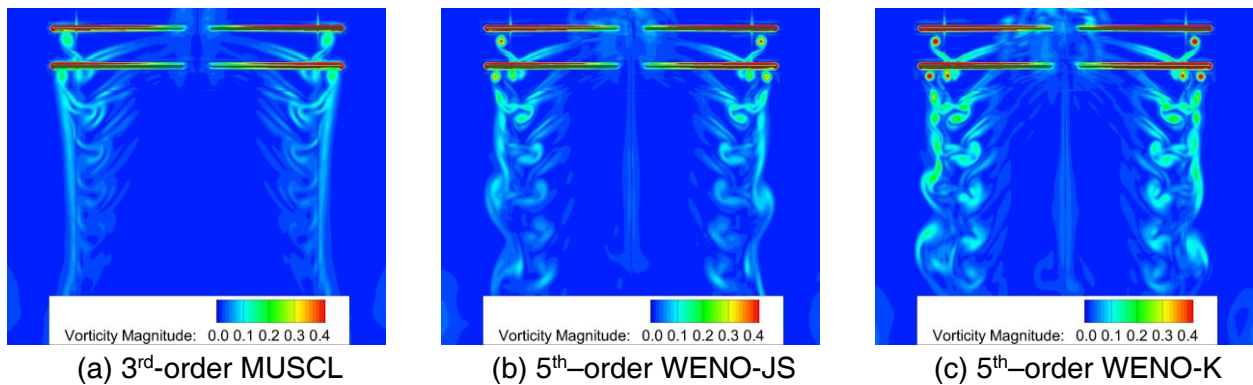
Figure 7 Comparison of vorticity contours on cutting plane parallel to chord length and passing through the shaft of rotor (θ=6°).

Figure 8 and Figure 10 show the comparison of blade-tip vortices visualized by iso-surface of q-criterion (q=0.01) and contours of vorticity magnitude at pitch angle of 9° and 12°. The conclusions are basically consistent with the results at 6° pitch angle. With the increase of the pitch angle, the blade-tip vortex become more intensive and move downward faster. Figure 9 and Figure 11 show the instantaneous vorticity contours. It can be seen that the WENO-K scheme can not only keep the blade-tip vortex to a bigger wake age, but also capable of capturing unsteady interference such as BVIs and vortex-vortex interaction between the wake of upper and lower rotor.

| (a) 3rd-order MUSCL | (b) 5th–order WENO-JS | (c) 5th–order WENO-K |
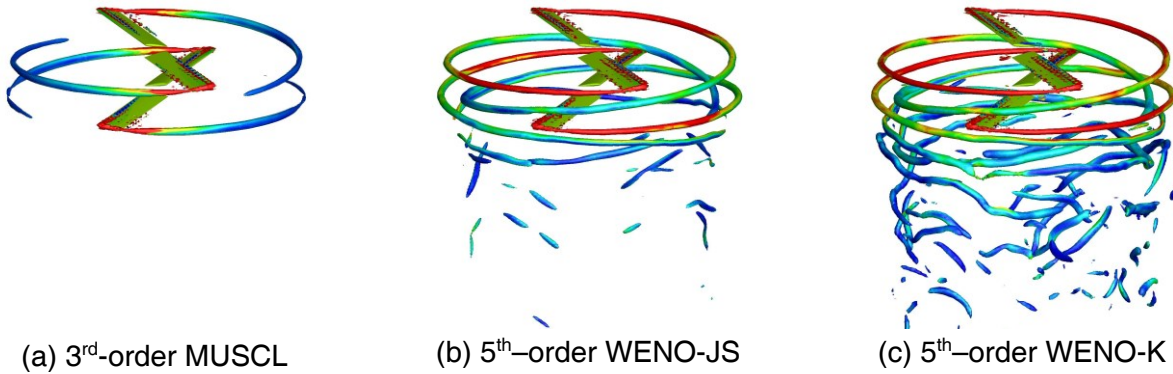
Figure 8 Comparison of tip vortex for coaxial rotor in hover (θ=9°). Vortices rendered with the iso-surface of q-criterion and contours of vorticity magnitude.

| (a) 3rd-order MUSCL | (b) 5th–order WENO-JS | (c) 5th–order WENO-K |
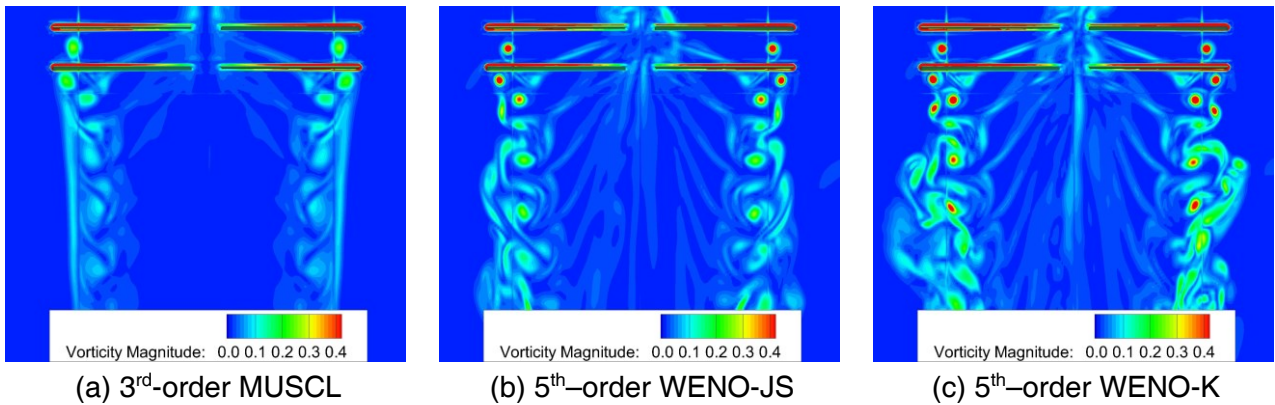
Figure 9 Comparison of vorticity contours on cutting plane parallel to chord length and passing through the shaft of rotor (θ=9°).

Figure 10 and Figure 11 show the vortex structure at pitch angle of 12°, in which WENO-K scheme gives the most detailed and clear unsteady evolution of vortex structure. Figure 12 shows the evolution of tip vortex structure obtained by using WENO-K scheme. Blade-tip vortices from both the upper and the lower rotors transports downward and paring with each other, then the paired vortices coalesce as a single vortical structure. The formation of the large vortical structure marks the end of contraction of wake, and in fact, it also marks the beginning of an expansion in the diameter of the wake as these structures continue to convect downstream of the rotor. Eventually, these structures are themselves torn apart, through their own mutual interaction, to form the turbulence field of highly disordered, low-level vorticity in the far-wake.

| (a) 3rd-order MUSCL | (b) 5th–order WENO-JS | (c) 5th–order WENO-K |
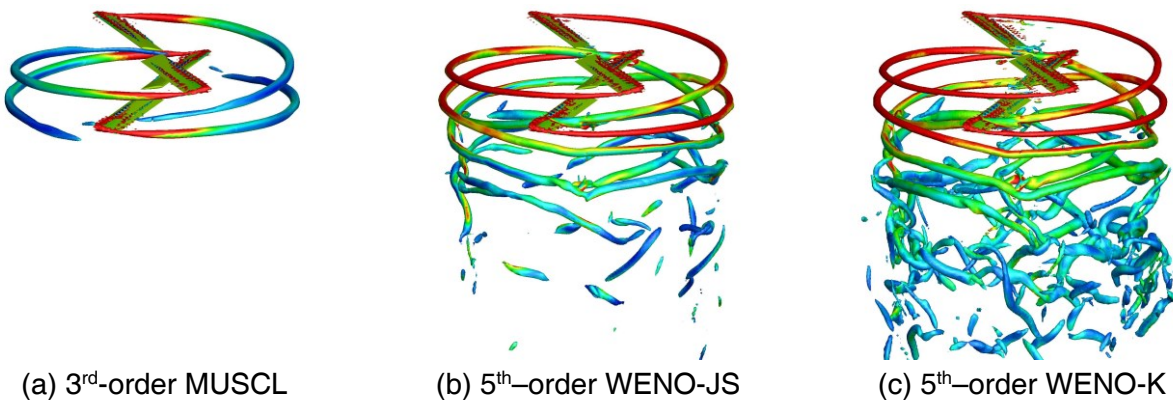
Figure 10 Comparison of tip vortex for coaxial rotor in hover (θ=12°). Vortices rendered with the iso-surface of q-criterion and contours of vorticity magnitude.

9

| (a) 3rd-order MUSCL | (b) 5th–order WENO-JS | (c) 5th–order WENO-K |
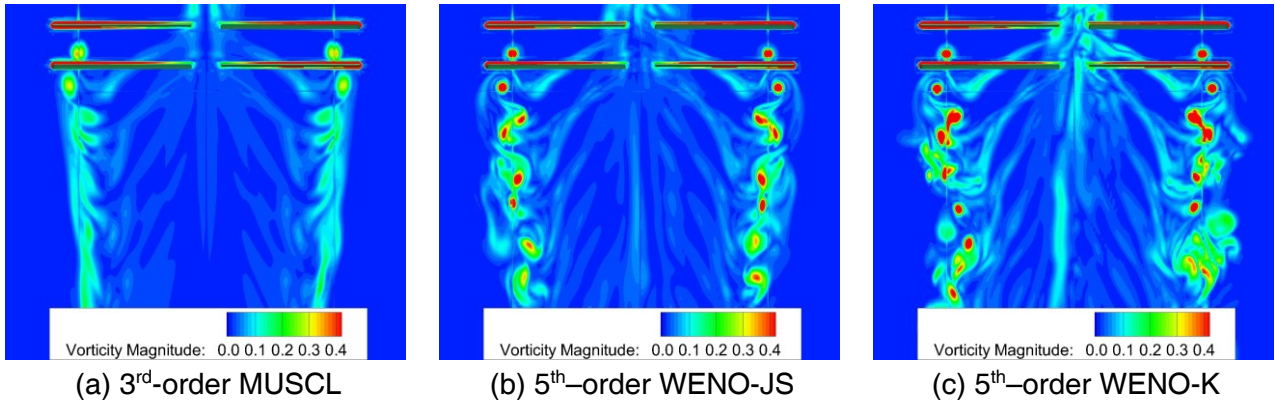
Figure 11 Comparison of vorticity contours on cutting plane parallel to chord length and passing through the shaft of rotor (θ=12°).
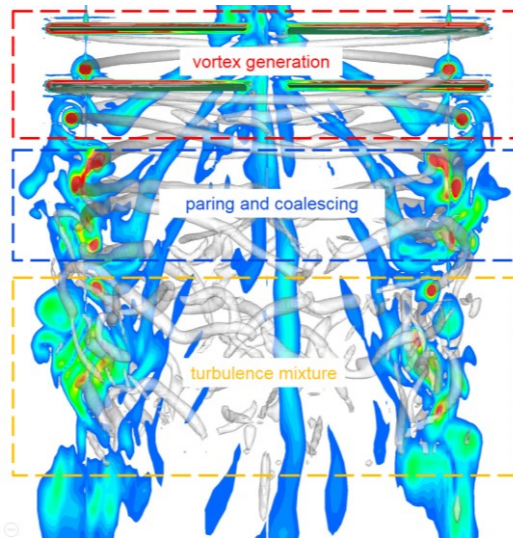
Figure 12 Evolution of tip vortex structure for coaxial rotor (WENO-K scheme, θ=12°).

3.3 Analysis of BVI phenomenon

Figure 13 presents the temporal C_T variation of the coaxial system over a revolution. The C_T of coaxial rotor in hover shows periodic unsteady fluctuations while that of the single rotor in hover almost keep stable. Thrust of lower rotor is smaller than that of the upper rotor due to the downwash of the upper rotor. The period is about 90°, as the blades meet 4 times over a revolution. C_T of the coaxial rotor gradually increase when the blades approach, then rapidly drop and increase again. When the upper and lower rotors meet with each other, the thickness effect leads to a sudden drop in the thrust of upper rotor, while the downwash load effect of upper rotor dominates a slow drop in the thrust of lower rotor. It can be seen from Figure 14 that BVI occurs four times on four positions (positions in the red circle) over a revolution between every blade of lower rotor and every blade-tip vortex of upper rotor. The BVI attach a certain effect on the pressure distribution of the blade on the positions where BVI occurs. Figure 15 gives the snapshot of wake vortex at the moment when BVI happens, the tip vortex of upper rotor collides with the blade of lower rotor and is divided into two segments.
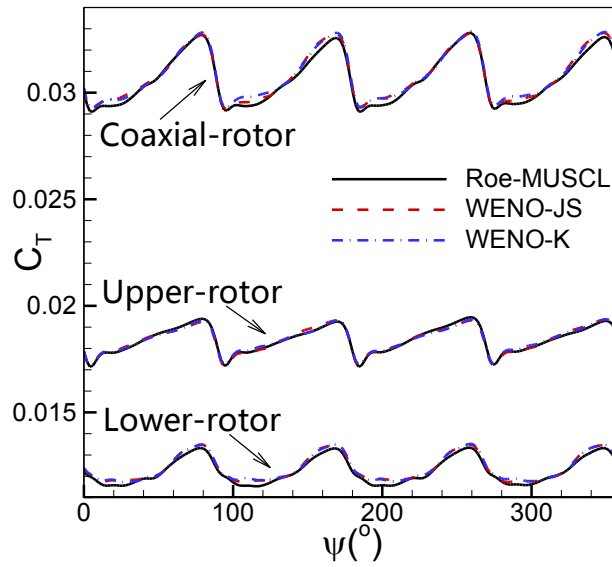
Figure 13 Variation of pull-down force coefficient with azimuth angle of coaxial twin rotors in hovering state (Ma=0.363, $\theta=12°$).

(a) 3rd-order MUSCL   (b) 5th–order WENO-JS   (c) 5th–order WENO-K
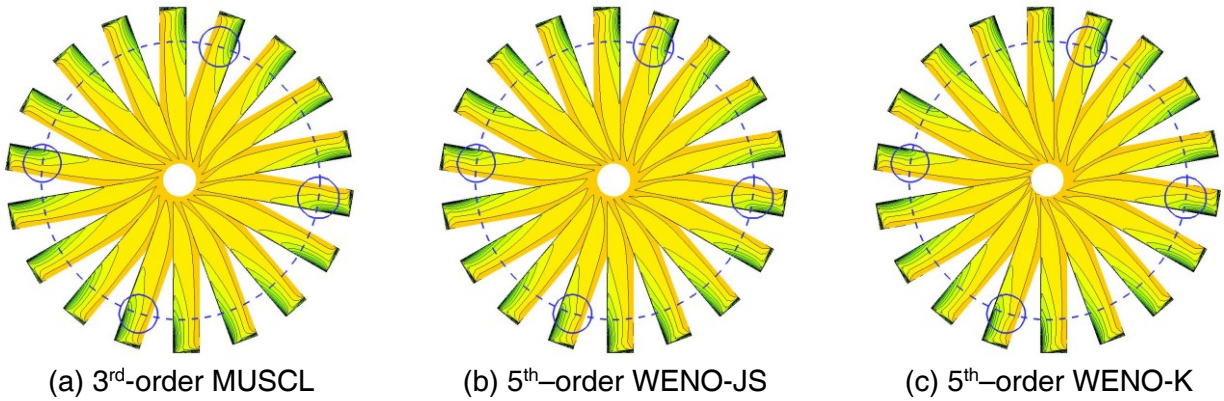
Figure 14 Surface pressure contours of lower rotor blades of coaxial twin rotors in hovering state calculated in different numerical formats (Ma=0.363, $\theta=12°$).
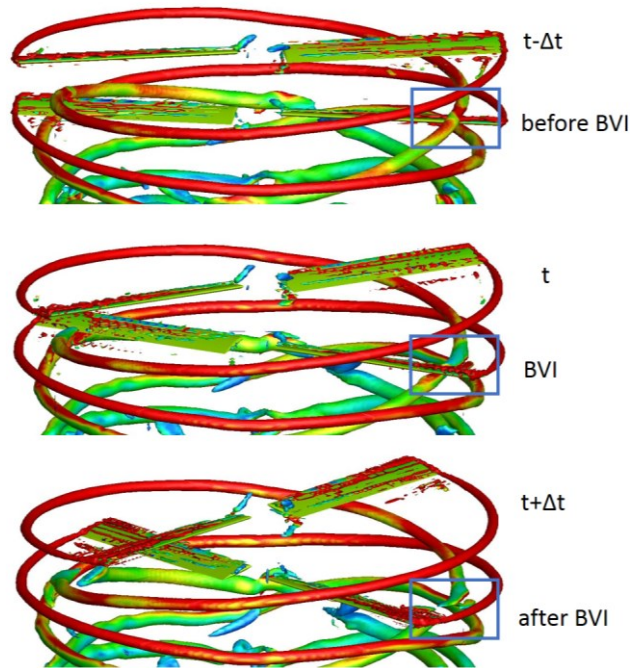
Figure 15 Visualization of tip vortex at the moment of BVI for coaxial rotor (Ma=0.363, $\theta=12°$, 5th WENO-K scheme)

11

Figure 16 shows the pressure distribution along the 1/4 chord line of lower rotor blade when the BVI occurs. The position surrounded by black rectangle is the area that is affected by BVI. Since MUSCL scheme does not capture BVI, it is considered that the pressure distribution calculated by MUSCL scheme is not affected by BVI. Both WENO-JS and WENO-K schemes can capture BVI, so the blade pressure distribution has been significantly disturbed. Among them, the disturbance calculated by WENO-K scheme is the most obvious. This is because WENO-K scheme features less dissipation and is capable of preserving more intensive blade-tip vortex. It is obvious that BVI could cause high-frequency pressure pulsation on the lower rotor blade and therefore affect aerodynamic and noise characteristics of coaxial rotor, and the high-order and low-dissipation WENO-K scheme is capable of giving a more accurate evaluation of this influence.
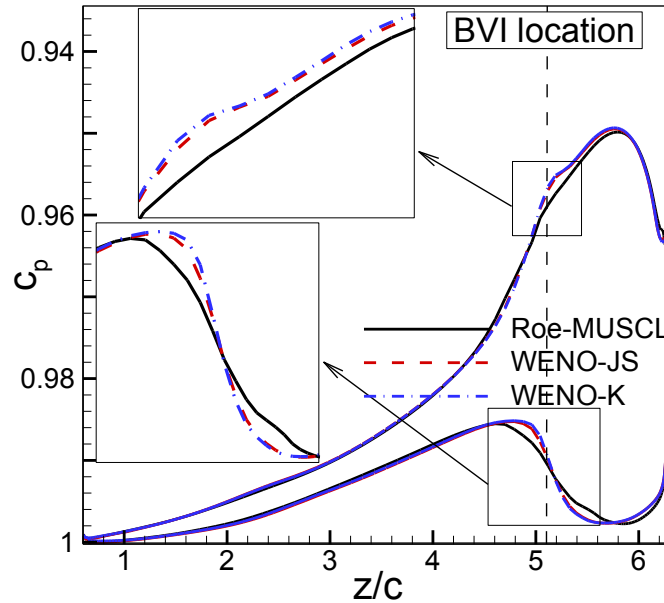
Figure 16 Pressure distribution on the 1/4 chord of the blade where the BVI occurs (Ma=0.363, θ=12°).

4. Conclusion

A computational study on blade-tip vortex structure and BVI for coaxial rotors in hover using a novel high-order and low-dissipation WENO-K scheme is conducted.

(1) The high-order WENO-K scheme that achieves innovative reconstruction utilizing the Gauss-kriging interpolation with an optimized hyper-parameter is extended to discretize URANS equations for complex flow dominated by unsteady vortices for coaxial rotors.

(2) The results of flow simulations on a four-blade coaxial rotor in hover demonstrate that the WENO-K scheme can effectively preserve vortex wake to a larger wake age, and capture more sophisticated evolution of unsteady vortex structures.

(3) High-order and low-dissipation WENO-K scheme contributes to capture of BVI, and therefore obtains an accurate evaluation of the impact of BVI on pressure distribution of blades.

5. Acknowledgements

6. Copyright Statement

7. Contact Author Email Address

Corresponding author: Han Shaoqiang, Email address: hanshaoqiang@scu.edu.cn

References

[1] Johnson W. Rotorcraft aeromechanics. Cambridge University Press, 2013.

[2] Rand O, Khromov V. Compound helicopter: insight and optimization. *Journal of the American Helicopter Society*, Vol. 60, No. 1, pp 1-12, 2015.

[3] Yeo H. Design and aeromechanics investigation of compound helicopters. *Aerospace Science and Technology*, Vol. 88, pp 158-173, 2019.

[4] Yang Z, Sankar L N, Smith M J, et al. Recent improvements to a hybrid method for rotors in forward flight[J]. Journal of Aircraft, 2002, 39(5):804-812.

[5] Nathan, Hariharan, Lakshmi N, Sankar. A review of computational techniques for rotor wake modeling. AIAA Paper 2000-0114, AIAA 38th Aerospace Sciences Meeting & Exhibit, Reno, NV, January 10-13.

[6] Kim H W, Brown R E. A Comparison of coaxial and conventional rotor performance[J]. *Journal of the American Helicopter Society*, 2009, 55(1):12004-1-12004-20.

[7] Ramasamy M, Leishman J G. A Reynolds number‑based blade tip vortex model[J]. *Journal of the American Helicopter Society*, 2007, volume 52(3):214-223(10).

[8] Martin P B, Pugliese G J, Leishman J G. High resolution trailing vortex measurements in the wake of a hovering rotor[J]. *Journal of the American Helicopter Society*, 2003, 48(1):39-52(14).

[9] Leishman J G, Ananthan S. An optimum coaxial rotor system for axial flight[J]. *Journal of the American Helicopter Society*, 2008, 53(4):366-381.

[10] Leishman J G. Aerodynamic performance considerations in the design of a coaxial proprotor[J]. *Journal of the American Helicopter Society*, 2009, 54(1):12005-1-12005-14.

[11] Syal M, Leishman J G. Aerodynamic optimization study of a coaxial helicopter rotor[J]. *Journal of the American Helicopter Society*, 2012, 57(4).

[12] ANDREW M J. Coaxial rotor aerodynamics in hover[J].Vertica, 1981,5(2):163-172

[13] Bagai A, Leishman J G. Free‑Wake analysis of tandem, tilt‑rotor and coaxial rotor configurations[J]. *Journal of the American Helicopter Society*, 1996, 41(3):196-207.

[14] Kim H W, Brown R E. A rational approach to comparing the performance of coaxial and conventional rotors[J]. *Journal of the American Helicopter Society*, 2009, 55(55):12003-1-12003-9.

[15] Kim H W, Brown R E. Modelling the aerodynamics of coaxial helicopters – from an isolated rotor to a complete aircraft[M]. EKC2008 Proceedings of the EU-Korea Conference on Science and Technology. Springer Berlin Heidelberg, 2008:45-59.

[16] Barbely, N. and Komerath, N. Coaxial rotor flow phenomena in forward flight, SAE Technical Paper 2016-01-2009, 2016.

[17] Xu H Y, Ye Z Y. Coaxial rotor helicopter in hover based on unstructured dynamic overset grids[J]. *Journal of Aircraft*, 2015, 47(5):1820-1824.

[18] Xu H Y, Ye Z Y. Numerical simulation of unsteady flow around forward flight helicopter with coaxial rotors[J]. *Chinese Journal of Aeronautics*, 2011, 24(1):1-7.

[19] Ye L, Xu G H. Calculation on flow field and aerodynamic force of coaxial rotors in hover with CFD method. *Acta Aerodynamica Sinica*, 2012, 30(4):437-442.(In Chinese)

[20] Zhu Z, Zhao Q J, Li P. Unsteady flow interaction mechanism of coaxial rigid rotors in hover. Acta *Aeronautica et Astronautica Sinica*, 2016(02):568-578. (In Chinese)

[21] Chiu IT, Meakin R. On automating domain connectivity for overset grids. *AIAA paper*, 1995-0854, 1995.

[22] Han S, Wenping S, Zhonghua H A N. A novel high-order scheme for numerical simulation of wake flow over helicopter rotors in hover. *Chinese Journal of Aeronautics*, 2021.

[23] Han S Q, Song W P, Han Z H. An improved WENO method based on Gauss-kriging reconstruction with an optimized hyper-parameter. *Journal of Computational Physics*, 422: 109742, 2020.

[24] AVAT E F, Toro B. Finite-volume WENO schemes for three-dimensional conservation laws[J]. *Journal of Computational Physics*, 2004, 201(1):238-260.

[25] Shen Y, Zha G, Wang B. Improvement of stability and accuracy for weighted essentially nonoscillatory scheme[J]. *AIAA Journal*, 2009.

[26] Roe PL. Approximate Riemann solvers, parameter vectors, and difference schemes. *Journal of Computational Physics*. Vol. 43, pp 357–372, 1981.

[27] Jiang G S, Shu C W. Efficient implementation of weighted ENO schemes. *Journal of Computational Physics*, Vol. 126, No. 1, pp 202-228, 1996.

[28] AVAT, BEFT. Finite-volume WENO schemes for three-dimensional conservation laws. *Journal of*

Computational Physics, Vol. 201, No. 1, pp 238-260, 2004.

[29]Hwang J Y, Kwon O J. Assessment of S-76 rotor hover performance in ground effect using an unstructured mixed mesh method. *Aerospace science and technology*, Vol. 84, pp 223-236, 2019.

[30]Xu L, Weng PF. High order accurate and low dissipation method for unsteady compressible viscous flow computation on helicopter rotor in forward flight. *Journal of Computational Physics*, Vol. 258, pp 470-488, 2014.

[31]Liao F. Efficient high-order high-resolution methods and the applications. Northwestern Polytechnical University, 2017 [in Chinese].

[32]Fu W, Ma J, Li J. Investigation of rotor tip vortex in hover based on IDDES methods. *Journal of Northwestern Polytechnical University*, Vol. 37, No. 1, pp 195-202, 2019.

[33]Coleman C P. A Survey of theoretical and experimental coaxial rotor aerodynamic research, NASA TP-3675, National Aeronautics and Space Administration, Ames Research Center, Moffett Field, CA, March 1997.